

Bias-Insensitive GaAsSb/InP CC-MUTC Photodiodes for mmWave Generation up to 325 GHz

Jesse S. Morgan^{ID}, Member, IEEE, Fatemehsadat Tabatabaei^{ID}, Tasneem Fatema^{ID}, Graduate Student Member, IEEE, Chak Wah Tang^{ID}, Keye Sun^{ID}, Kei May Lau^{ID}, Life Fellow, IEEE, and Andreas Beling^{ID}, Senior Member, IEEE

Abstract—Back-illuminated GaAsSb/InP charge-compensated modified uni-traveling carrier (CC-MUTC) photodiodes (PDs) with 3-dB bandwidths above 110 GHz at 0 V and 125 GHz at -1.1 V, and 12 dB roll-off through 325 GHz are demonstrated. Millimeter wave output power of +5.8 dBm at 100 GHz, +1.2 dBm at 160 GHz, -3.1 dBm at 220 GHz, and -10.5 dBm at 300 GHz is shown. A new fabrication methodology for surface normal photodiodes that does not require an air bridge and reduces parasitic capacitance by $> 3\times$ from our previous devices is described. These photodiodes use a continuously graded doping in the absorber, and achieve high power performance both at zero-bias and low-bias, with a bias-insensitive responsivity of 0.11 A/W at 1550 nm wavelength.

Index Terms—CC-MUTC PD, high-speed-photodiodes, low-bias, millimeter-wave photonics, mmWave, Zero-bias.

I. INTRODUCTION

APPLICATIONS using photonic generation of radio frequency (RF) signals continue to move to higher frequencies, and high-speed photodiodes (PDs) continue to be a critical component in a wide range of these systems [1], [2], [3]. Analog photonics applications including radio-over-fiber and antenna remoting, require that photodiodes have high power handling capability and high linearity in order to maintain high RF gain and large spurious-free dynamic range [4], and CC-MUTC PDs are known to facilitate these requirements [5]. A narrow-bandgap absorber layer and a wide-bandgap electron drift (carrier collector) layer are the essential layers in all uni-traveling carrier (UTC) PDs [6]. In a UTC PD only fast electrons transit through the drift layer resulting in a fast response [7]. Situated close to

Manuscript received 20 April 2023; revised 4 July 2023; accepted 11 July 2023. Date of publication 26 July 2023; date of current version 2 December 2023. This work was supported by the National Science Foundation under Grant 2023775. (Jesse S. Morgan and Fatemehsadat Tabatabaei contributed equally to this work.) (Corresponding author: Andreas Beling.)

Jesse S. Morgan, Fatemehsadat Tabatabaei, Tasneem Fatema, Keye Sun, and Andreas Beling are with the Department of Electrical and Computer Engineering, University of Virginia, Charlottesville, VA 22903-1738 USA (e-mail: jsm2ne@virginia.edu; ft4xx@virginia.edu; tf4ev@virginia.edu; ks2kz@virginia.edu; ab3pj@virginia.edu).

Chak Wah Tang and Kei May Lau are with the Department of Electronic and Computer Engineering, Hong Kong University of Science and Technology, Kowloon, Hong Kong (e-mail: eewilson@ust.hk; eekmlau@ust.hk).

Color versions of one or more figures in this article are available at <https://doi.org/10.1109/JLT.2023.3298772>.

Digital Object Identifier 10.1109/JLT.2023.3298772

the highly-doped p-contact layer, photogenerated holes in the absorber layer respond quickly within the dielectric relaxation time [6]. Additionally, n-type doping in the drift layer helps to compensate for the space charge effect [8] and in a MUTC PD, a thin partly depleted absorber enhances responsivity without compromising bandwidth. Previous CC-MUTC PDs required additional layers including a step-graded doped partially depleted absorber [9], cliff layer [10], an electron blocking layer, and grading layers [11] to improve the device performance. In these previous designs, quaternary grading layers are used to promote the electron transition at the discontinuity in the conduction band that arises from type-I band alignment at the In-GaAs absorber layer and the InP drift layer heterointerface [11]. To enable more favorable carrier transport and to reduce the epitaxial layer complexity, GaAsSb with type-II band alignment at the absorber/drift layers can be used as the absorber. As a result, the quaternary grading layers are not required since the conduction band discontinuity at the heterointerface is removed [12]. Previously we showed that this approach can enable 66 GHz bandwidth at zero-bias [13].

In this work, we report a high power back-illuminated CC-MUTC PDs with type-II band alignment operating at zero bias and low bias, utilizing a new fabrication method for CC-MUTC PDs. Device structure, fabrication procedure, and device characterization are described. Compared with previous MUTC PD designs, we achieve high-speed, high-power performance with a simpler epitaxial layer structure that does not include an electron blocking layer, quaternary grading layers, or cliff layer. The PDs achieve a high zero-bias responsivity of 0.08 A/W and a responsivity of 0.11 A/W under -1 V and -1.8 V bias at 1550-nm, relative to other surface normal, 100-nm thick absorber layer designs [15]. We report the first photodiode demonstrating high-power performance in the millimeter wave (mmWave) spectrum under both, bias and zero-bias conditions, compared to previous designs which sacrificed performance for one over the other [16], [17], [18], [19].

II. DEVICE STRUCTURE AND FABRICATION

The epitaxial stack-up is shown in Fig. 1. The structure is grown by molecular beam epitaxy on a 500- μm thick, semi-insulating InP substrate. The 500-nm thick InP n-contact layer

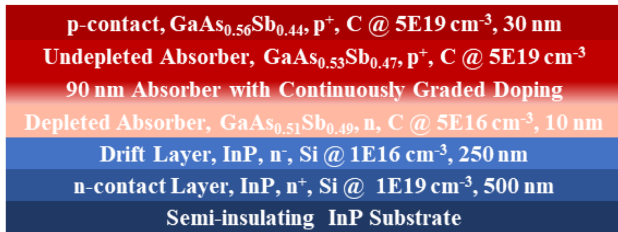
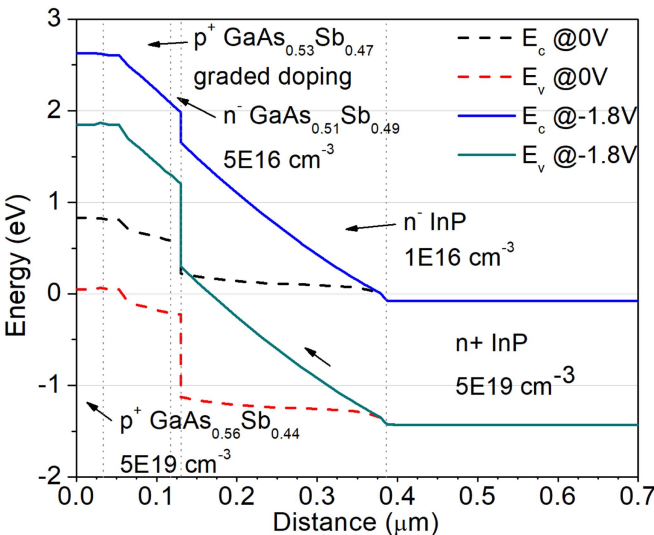


Fig. 1. Epitaxial stack-up for type-II CC-MUTC PD.

Fig. 2. Simulated energy band diagrams. The slope of the bands between $0.13 \mu\text{m}$ and $0.38 \mu\text{m}$ indicates that the drift layer is depleted at 0 V .

is doped with Si to a density of $1\text{E}19 \text{ cm}^{-3}$, followed by a 250-nm thick InP drift layer with Si doping density of $1\text{E}16 \text{ cm}^{-3}$. Above the drift layer is a 10-nm GaAs_{0.51}Sb_{0.49} depleted absorber C doped to a $5\text{E}16 \text{ cm}^{-3}$ density, followed by a continuously graded, 90-nm undepleted absorber, with final C doping density of $5\text{E}19 \text{ cm}^{-3}$ and composition of GaAs_{0.53}Sb_{0.47}. By removing abruptness in doping in the absorber, we can achieve a smoother electric field profile which could lead to a more efficient electron transport occurring at maximal drift velocity, making these devices faster than previous CC-MUTC PDs. Finally, above the absorber, is a heavily doped 30-nm thick GaAs_{0.56}Sb_{0.44} p-contact layer with C doping density of $5\text{E}19 \text{ cm}^{-3}$. Simulated band diagrams of the structure are shown in Fig. 2.

The PDs are fabricated using a double-mesa, contact lithography procedure with 5 photomasks. The surface normal PDs incorporate an SU8 planarization step similar to that first demonstrated in [20] for waveguide coupled photodiodes. P-metal was first deposited on the chip using electron beam deposition with a metal stack of Ti/Pt/Au/Ti, followed by an SiO₂ plasma-enhanced chemical vapor deposition (PECVD). The first photomask lithography designated the device p-mesa, which was reactively ion etched (RIE) into the SiO₂ hard mask, and then inductively-coupled plasma etched (ICP-RIE) down to the n-contact. The second lithography defined the n-mesa which was

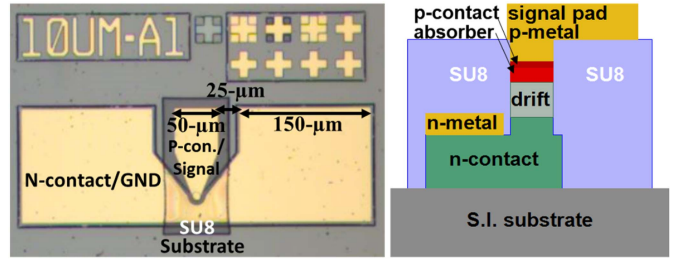
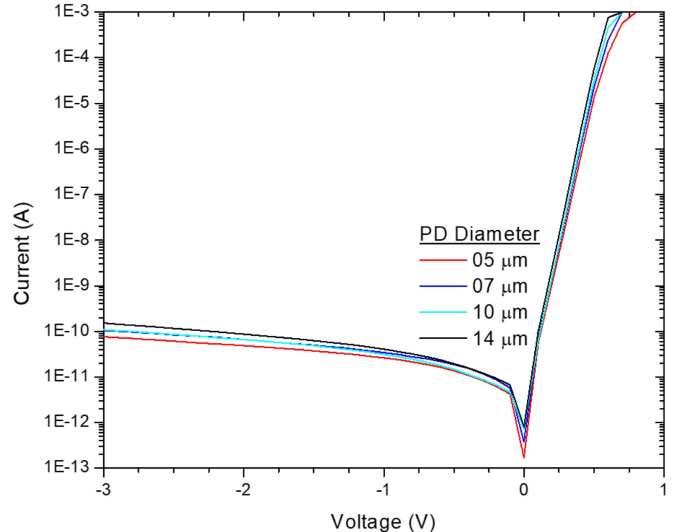
Fig. 3. Microscope image of completed $10\text{-}\mu\text{m}$ device (left) and middle side-slice view of device (right).

Fig. 4. Measured dark currents.

then ICP-RIE dry etched into the semi-insulating InP substrate. A AuGe/Ni/Au n-metal stack was then deposited, followed by lift-off. After a wet-etch to remove any remaining SiO₂, the next step was a planarization spin-on of SU8. The fourth lithography then defined the SU8 pad structure around the p-mesa. The SU8 was then RIE dry-etched using a combination of O₂ and SF₆ [21] until the top of the p-mesa was exposed, creating a pad for the signal metal to be deposited on while at the same time passivating the PD's p-mesa. The p-contact signal pad was fabricated on top of the p-mesa and SU8 layer. Finally, the backside of the chip was polished to minimize optical input coupling reflection. Fig. 3 shows a microscope image of a completed $10\text{-}\mu\text{m}$ PD (left) and a side illustration of the device (right).

The back-illuminated surface normal photodiodes with active area diameters of $5 \mu\text{m}$, $7 \mu\text{m}$, $10 \mu\text{m}$ and $14 \mu\text{m}$ were fabricated utilizing a $50\text{-}\Omega$ ground-signal-ground (GSG) coplanar waveguide (CPW). The CPW included a tapered signal and ground plane connecting the photodiode p-mesa and n-mesa to a $50\text{-}\mu\text{m}$ wide signal plane and $150\text{-}\mu\text{m}$ wide ground plane, respectively, with a $25\text{-}\mu\text{m}$ gap distance to maintain a broadband $50\text{-}\Omega$ characteristic impedance at the output of the photodiode from DC to 300 GHz. The signal pad was deposited on an $80\text{-}\mu\text{m}$ wide 980 nm-thick SU8 layer. I-V curves of the devices taken from -3 V to 1 V are shown in Fig. 4.

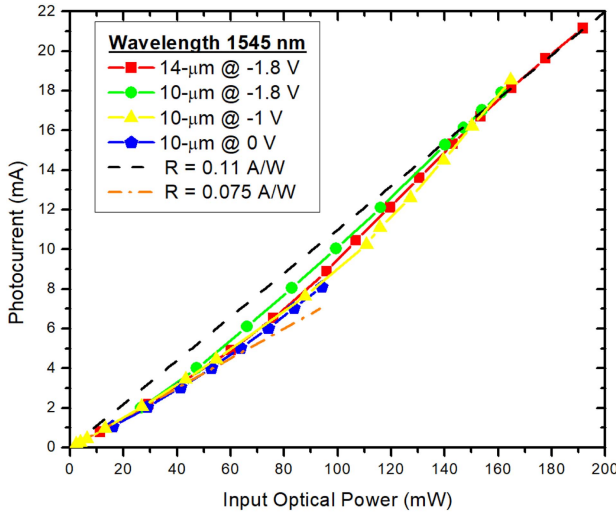


Fig. 5. Photocurrent versus input optical power at -1 V , -1.8 V , and 0 V bias.

III. CHARACTERIZATION

Dark current in the $5\text{-}\mu\text{m}$ PDs was as low as 76 pA , and 152 pA in the $14\text{-}\mu\text{m}$ devices at -3 V bias (Fig. 4). Shown in Fig. 5, the responsivity measured at 0 V and at -1 V and -1.8 V bias, using an $8\text{-}\mu\text{m}$ spot-size collimated fiber at 1545 nm wavelength. At 0 V bias the responsivity is 0.08 A/W , with a relatively flat response. The responsivity for both PDs at -1 V and -1.8 V is 0.11 A/W which shows the responsivity is not bias-dependent in this range. As seen in Fig. 5, at low optical power the responsivity is $\sim 0.075\text{ A/W}$, then with increasing optical power, the responsivity increases until flattening out at 0.11 A/W in both devices. The dependency on optical power could be attributed to the fact that there is no blocking layer, and at low optical power, with low DC photocurrent, the self-induced field in the undepleted absorber is also low [22]. This means electrons can diffuse more easily into the p-contact and recombine, thus not contributing to the DC photocurrent. With increasing optical power, the self-induced field increases as well, supporting electron transit to the drift layer where they can then be collected. These responsivity measurements were taken on devices without anti-reflection coating (ARC) and so with ARC the PDs should achieve $\sim 27\%$ improvement in responsivity.

Scattering parameter S_{11} measurements were performed to characterize the PDs' impedance from 10 MHz to 110 GHz . The circuit model is shown in Fig. 6(a). The PD is modeled as a current source, I_{PD} , in parallel with a junction capacitance, C_{pn} , junction resistance, R_{pn} , and series resistance R_s . The Method of Moments modeled CPW is also included in the circuit model and the external load is represented by R_{load} ($50\ \Omega$). Using this circuit model, S_{11} is fitted to the measured data, and the results are shown for a $10\text{-}\mu\text{m}$ PD in Fig. 6(b) and $05\text{-}\mu\text{m}$ PD in Fig. 6(c). The extracted junction capacitances at 0 V and -1 V for all devices is shown with the calculated values vs. PD active area in Fig. 7. In the parallel plate capacitor equation shown in Fig. 7, ϵ_0 is the vacuum permittivity, ϵ_r is the dielectric constant for InP of 9.6 , A_{PD} is the active area of the photodiode, and d_{dep} is the nominal width of the depletion region (250 nm). A

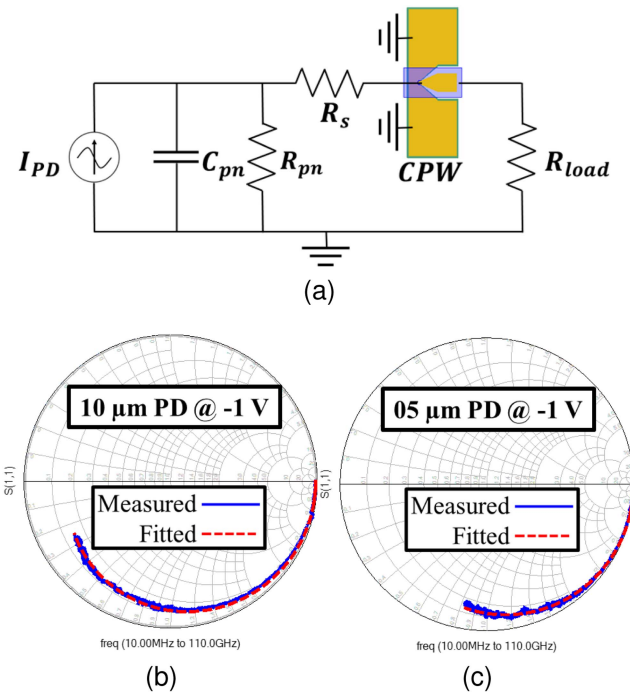


Fig. 6. Equivalent circuit model for S_{11} fitting (a), measured vs. fitted S_{11} results for a $05\text{-}\mu\text{m}$ (b) and $10\text{-}\mu\text{m}$ PD (c).

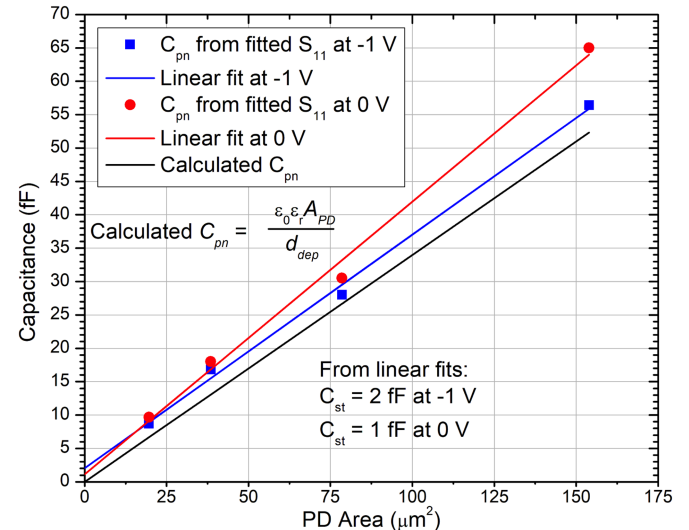


Fig. 7. Junction capacitance vs. PD active area for calculated (black), and S_{11} fitting extracted values at -1 V (blue) and 0 V (red).

linear fit of the extracted values shows that the stray capacitance C_{st} (at PD Area = 0) in the devices was between 1 and 2 fF . Compared to our previous flip-chip bonded PDs with an air-bridge, the new SU8 planarization fabrication procedure reduces stray capacitance by $> 3X$ [16]. Series resistance in the PDs scaled inversely with device active area, and was found to be $14\text{-}\Omega$ in the $10\text{-}\mu\text{m}$ devices and $50\text{-}\Omega$ in the $05\text{-}\mu\text{m}$ devices. A summary of the extracted and calculated values can be seen in Table I. The junction resistance is of the order of 100's of $k\Omega$'s and is thus neglected.

TABLE I
CALCULATED, FITTED, AND MEASURED PARAMETERS

PD Ø	C_{pn} Calc.	C_{pn} S11 Fit at -1 (0) V	R_s S11 Fit	$f_{RC} = (2\pi(R_S + R_{load})(C_{pn} + C_{st}))^{-1}$ at -1 (0) V	Measured f_{3dB} at -1.1 (0) V
05-µm	7 fF	9 (10) fF	50 Ω	145 (133) GHz	125 (>110) GHz
07-µm	13 fF	17 (18) fF	26 Ω	110 (105) GHz	100 (93) GHz
10-µm	27 fF	28 (30) fF	14 Ω	83 (78) GHz	75 (70) GHz
14-µm	52 fF	56 (65) fF	10 Ω	46 (40) GHz	36 (40) GHz

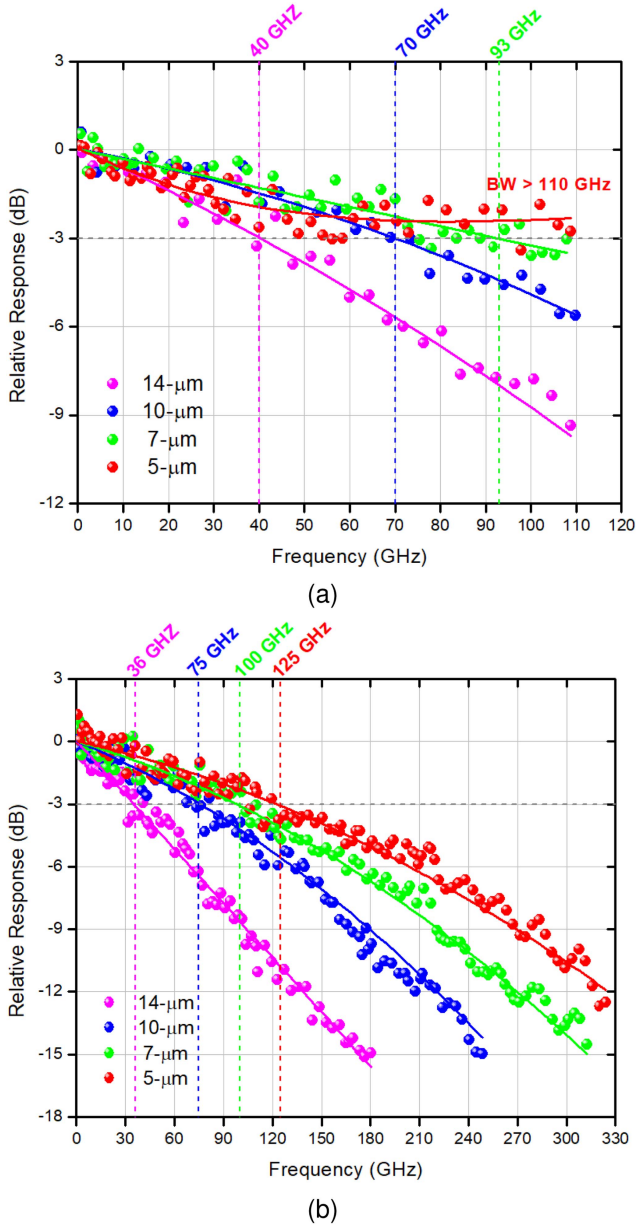


Fig. 8. Bandwidth measured with an optical heterodyne setup at 0 V bias and 0.5 mA from DC-110 GHz (a), and at -1.1 V and 2.5 mA from DC-325 GHz (b). Solid lines show polynomial fitting curves.

In order to investigate the performance of the PDs at zero and low bias, bandwidth was measured from DC-110 GHz at 0 bias and 0.5-mA, and from DC-325 GHz at -1.1 V bias and 2.5-mA, as shown in Fig. 8. It should be mentioned that zero-bias PDs relax the need for a DC bias circuit. Also, driving

PDs at low bias can reduce power consumption. In Fig. 8(a), using a polynomial fitting, the 5-µm PD achieves a bandwidth of greater than 110 GHz, and the 7, 10, and 14-µm PDs achieve bandwidths of 93, 70, and 40 GHz, respectively. In Fig. 8(b), the polynomial fitting shows the 5, 7, 10, and 14-µm PDs achieving 3-dB bandwidths of 125, 100, 75, and 36 GHz, respectively. These results show that the devices perform at high speed at both 0 bias and at low bias operation. A summary of the measured bandwidths f_{3dB} and the calculated resistance-capacitance (RC) limited bandwidths f_{RC} from fitted parameters is shown in Table I. We also extracted the transit time limited bandwidths from the measurements of 05-µm, 07-µm, and 10-µm diameter PDs using the procedure described in [12]. At -1.1 V, we found 207 GHz, which is close to the calculated transit time limited bandwidth of 245 GHz using the following equation,

$$f_t = \frac{3.5\bar{v}}{2\pi d_{dep}}, \quad (1)$$

Equation (1) considers only electron transport in the drift layer where \bar{v} is the electron drift velocity (1.1×10^7 cm/s) [28] and $d_{dep} = 250$ nm. The result suggests that electron drift dominates the transit time response, and, owing to the continuously graded doping in our thin undepleted absorber, bandwidth limitations due to electron diffusion play only a minor role. At 0 V, the extracted transit time was 158 GHz. Most likely, the reduction can be explained by a lower electron velocity in the drift layer in addition to contributions from electron diffusion in the undepleted absorber.

In order to determine the optimum bias voltage for saturation power measurements, the RF power near the saturation point was measured over a range of voltages at 160 GHz, as shown in Fig. 9, where at -1.8 V bias, the maximum RF power output is reached in both devices under test. The decreasing power output at higher reverse bias potentially comes from a reduced velocity overshoot in the InP collector. At low bias, the space charge effect limits the RF output power. The maximum output power measured at -1.8 V at 100 GHz, 160 GHz, 220 GHz, and 300 GHz is shown in Fig. 10. At 100 GHz, a 14-µm PD reaches 5.8 dBm at 37.5 mA, at 160 GHz a 10-µm PD reaches 1.2 dBm at 25.1 mA, a 10-µm PD reaches -3.1 dBm at 24.7 mA at 220 GHz, and at 300 GHz a 10-µm PD reaches -10.5 dBm at 25.3 mA. It should be mentioned that we measured PDs with different diameters at these frequencies, however, here we show only data from the PDs that reached the maximum output power.

RF power was also measured at 0 V bias, as shown in Fig. 11. A 10-µm PD reaches -9.3 dBm at 7 mA at 100 GHz, -12.2 dBm at 8 mA at 160 GHz, -14.3 dBm at 7.6 mA at 220 GHz, and a 07-µm PD reaches -19.3 dBm at 4.9 mA at 300 GHz. It is

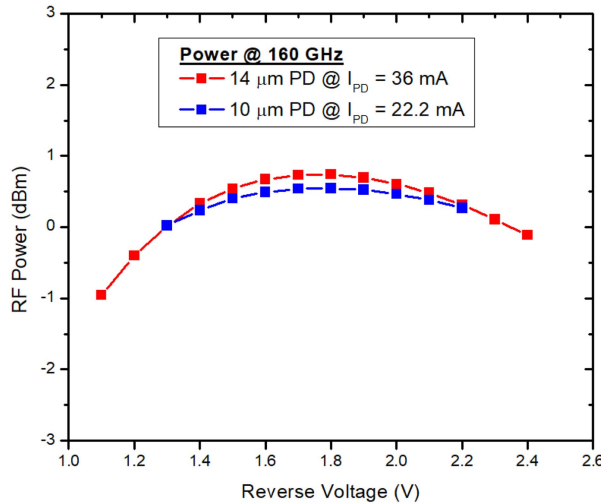


Fig. 9. RF power vs. bias near saturation for 10- μm (blue) and 14- μm (red) PDs.

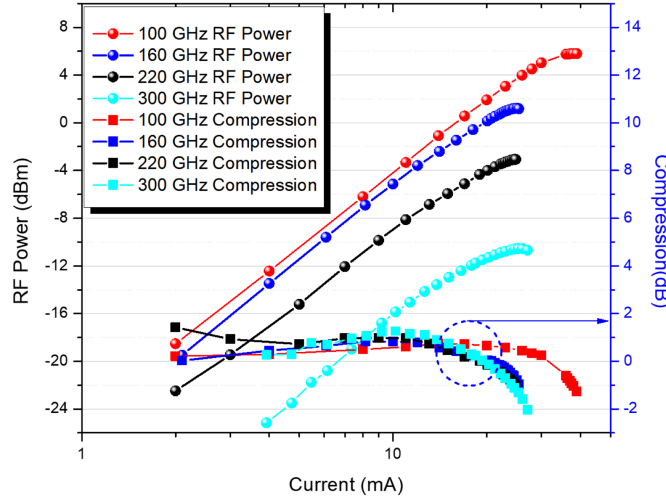


Fig. 10. RF power measured at -1.8 V bias at 100 GHz for a 14- μm PD, and at 160, 220, and 300 GHz for a 10- μm PD.

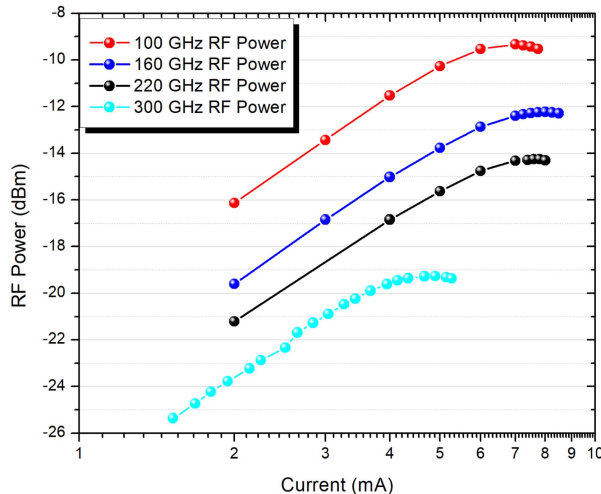


Fig. 11. RF power measured at 0 V bias at 100, 160, and 220 GHz for a 10- μm PD, and at 300 GHz for a 07- μm PD.

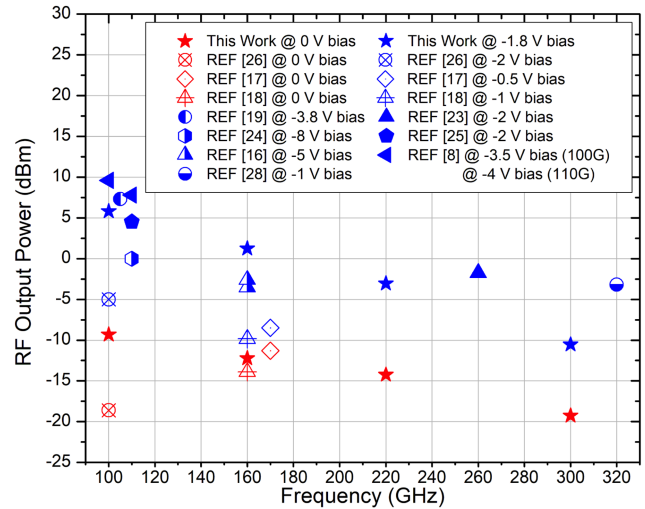


Fig. 12. Output power in mmWave spectrum for single PDs, CW excitation, at $50\ \Omega$ load, at zero-bias (red points) and non-zero bias (blue points) conditions.

worth noting that previous zero bias, flip-chip bonded PDs were reported only up to 170 GHz [17], and for the first time we demonstrate zero-bias PDs suitable for 300 GHz detection.

IV. CONCLUSION

We have designed high-speed, high-power MUTC PDs operating at 1550 nm, using a new epitaxial stack and device design, and new fabrication procedure for back-illumination. These PDs achieve 3-dB bandwidths of 125 GHz at -1.1 V bias, and greater than 110 GHz at 0 V bias. They achieve a flat roll-off of 12 dB up to 325 GHz and a responsivity of $0.11\ \text{A/W}$ without ARC. The type-II band alignment at the absorber/drift layer interface with a lightly doped drift layer enables high power levels in the mmWave band as shown in Fig. 12 both at low bias and zero bias operating points. Compared to other broadband PDs reported in the literature, our PDs offer robust performance with high power outputs at lower bias and are the first PDs to have detection capability at 300 GHz and zero bias.

REFERENCES

- [1] A. Beling et al., "High-speed integrated photodiodes," in *Proc. 24th OptoElectronics Commun. Conf. Int. Conf. Photon. Switching Comput.*, Fukuoka, Japan, 2019, pp. 1–3.
- [2] S. Dulme et al., "300 GHz photonic self-mixing imaging-system with vertical illuminated triple-transit region photodiode Terahertz emitters," in *Proc. Int. Topical Meeting Microw. Photon.*, 2019, pp. 1–4.
- [3] H. Ito et al., "Photonic millimetre-wave emission at 300 GHz using an antenna-integrated uni-travelling-carrier photodiode," *Electron. Lett.*, vol. 38, pp. 989–990, Sep. 2002.
- [4] V. Ulrich, K. Williams, and J. McKinney, *Fundamentals of Microwave Photonics*. Hoboken, NJ, USA: Wiley, 2015.
- [5] K. Sun and A. Beling, "High-speed photodetectors for microwave photonics," *Appl. Sci.*, vol. 9, 2019, Art. no. 623.
- [6] H. Ito, S. Kodama, Y. Muramoto, T. Furuta, T. Nagatsuma, and T. Ishibashi, "High-speed and high-power output InP-InGaAs unidirectional-carrier photodiodes," *IEEE J. Sel. Topics Quantum Electron.*, vol. 10, no. 4, pp. 709–727, Jul./Aug. 2004.
- [7] T. Ishibashi, S. Kodama, N. Shimizu, and T. Furuta, "High-speed response of uni-travelling-carrier photodiodes," *Japanese J. Appl. Phys.*, vol. 36, 1997, Art. no. 6263.

- [8] Q. Li et al., "High-power flip-chip bonded photodiode with 110 GHz bandwidth," *J. Lightw. Technol.*, vol. 34, no. 9, pp. 2139–2144, May 2016.
- [9] B. Wang et al., "Towards high-power, high-coherence, integrated photonic mmWave platform with microcavity solitons," *Light: Sci. Appl.*, vol. 10, 2021, Art. no. 4.
- [10] N. Shimizu, N. Watanabe, T. Furuta, and T. Ishibashi, "InP-InGaAs uni-traveling-carrier photodiode with improved 3-dB bandwidth of over 150 GHz," *IEEE Photon. Technol. Lett.*, vol. 10, no. 3, pp. 412–414, Mar. 1998.
- [11] X. Xie, J. Zang, A. Beling, and J. Campbell, "Characterization of amplitude noise to phase noise conversion in charge-compensated modified untraveling carrier photodiodes," *J. Lightw. Technol.*, vol. 35, no. 9, pp. 1718–1724, May 2017.
- [12] L. Zheng et al., "Demonstration of high-speed staggered lineup GaAsSb-InP untraveling carrier photodiodes," *IEEE Photon. Technol. Lett.*, vol. 17, no. 3, pp. 651–653, Mar. 2005.
- [13] F. Yu, K. Sun, Q. Yu, and A. Beling, "High-speed evanescently-coupled waveguide type-II MUTC photodiodes for zero-bias operation," *J. Lightw. Technol.*, vol. 38, no. 24, pp. 6827–6832, Dec. 2020.
- [14] B. Tossoun, J. Zang, S. J. Addamane, G. Balakrishnan, A. L. Holmes, and A. Beling, "InP-based waveguide-integrated photodiodes with In-GaAs/GaAsSb type-II quantum wells and 10-GHz bandwidth at 2- μ m wavelength," *J. Lightw. Technol.*, vol. 36, no. 20, pp. 4981–4987, Oct. 2018.
- [15] A. M. Arabhavi et al., "Type-II GaInAsSb/InP uniform absorber high speed uni-traveling carrier photodiodes," *J. Lightw. Technol.*, vol. 39, no. 7, pp. 2171–2176, Apr. 2021.
- [16] J. S. Morgan et al., "High-power flip-chip bonded modified uni-traveling carrier photodiodes with 2.6 dBm RF output power at 160 GHz," in *Proc. IEEE Photon. Conf.*, 2018, pp. 1–2.
- [17] J.-M. Wun, R.-L. Chao, Y.-W. Wang, Y.-H. Chen, and J.-W. Shi, "Type-II GaAs_{0.5}Sb_{0.5}/InP uni-traveling carrier photodiodes with sub-Terahertz bandwidth and high-power performance under zero-bias operation," *J. Lightw. Technol.*, vol. 35, no. 4, pp. 711–716, Feb. 2017.
- [18] J. Wun, Y. Zeng, and J. Shi, "GaAs_{0.5}Sb_{0.5}/InP UTC-PD with graded-bandgap collector for zero-bias operation at Sub-THz regime," in *Proc. Opt. Fiber Commun. Conf.*, 2016, Paper Tu2D.4.
- [19] J. Li et al., "Ultrafast dual-drifting layer uni-traveling carrier photodiode with high saturation current," *Opt. Exp.*, vol. 24, 8420–8428, 2016.
- [20] B. Tossoun, J. Morgan, and A. Beling, "Ultra-low capacitance, high-speed integrated waveguide photodiodes on InP," in *Proc. OSA Adv. Photon. Congr.*, 2019, Paper IT3A.6.
- [21] K. Rasmussen, S. S. Keller, F. Jensen, A. Jorgensen, and O. Hansen, "SU-8 etching in inductively coupled oxygen plasma," *Microelectronic Eng.*, vol. 112, pp. 35–40, 2013.
- [22] N. Shimizu, N. Watanabe, T. Furuta, and T. Ishibashi, "Improved response of uni-traveling-carrier photodiodes by carrier injection," *Japanese J. Appl. Phys.*, vol. 37, pp. 1424–1426, 1998.
- [23] J. Wun, C. Lai, N. Chen, J. Bowers, and J. Shi, "Flip-chip bonding packaged THz photodiode with broadband high-power performance," *IEEE Photon. Technol. Lett.*, vol. 26, no. 24, pp. 2462–2464, Dec. 2014.
- [24] V. Rymanov, A. Stöhr, S. Dülme, and T. Tekin, "Triple transit region photodiodes (TTR-PDs) providing high millimeter wave output power," *Opt. Exp.*, vol. 22, pp. 7550–7558, 2014.
- [25] A. Stöhr et al., "Millimeter-wave photonic components for broadband wireless systems," *IEEE Trans. Microw. Theory Techn.*, vol. 58, no. 11, pp. 3071–3082, Nov. 2010.
- [26] T. Umezawa et al., "Zero-bias operational ultra-broadband UTC-PD above 110 GHz for high symbol rate PD-array in high-density photonic integration," in *Proc. Opt. Fiber Commun. Conf. Exhib.*, 2015, pp. 1–3.
- [27] K. Kato, H. Susumu, K. Kawano, and A. Kozen, "Design of ultrawideband, high-sensitivity pin photodetectors," *IEICE Trans. Electron.*, vol. 76, pp. 214–221, 1993.
- [28] J.-M. Wun, Y.-W. Wang, and J.-W. Shi, "Ultra-fast uni-traveling carrier photodiodes with GaAs_{0.5}Sb_{0.5}/In_{0.53}Ga_{0.47}As Type-II hybrid absorbers for high-power operation at THz frequencies," *IEEE J. Sel. Topics Quantum Electron.*, vol. 24, no. 2, Mar./Apr. 2018, Art. no. 8500207.